



HAL
open science

Molecular Dynamics Simulation of Water Confinement in Disordered Aluminosilicate Subnanopores

Takahiro Ohkubo, S. Gin, Marie Collin, Yasuhiko Iwadate

► **To cite this version:**

Takahiro Ohkubo, S. Gin, Marie Collin, Yasuhiko Iwadate. Molecular Dynamics Simulation of Water Confinement in Disordered Aluminosilicate Subnanopores. *Scientific Reports*, 2017, 8, pp.3761. 10.1038/s41598-018-22015-3 . cea-02421746

HAL Id: cea-02421746

<https://cea.hal.science/cea-02421746>

Submitted on 12 Jun 2020

HAL is a multi-disciplinary open access archive for the deposit and dissemination of scientific research documents, whether they are published or not. The documents may come from teaching and research institutions in France or abroad, or from public or private research centers.

L'archive ouverte pluridisciplinaire **HAL**, est destinée au dépôt et à la diffusion de documents scientifiques de niveau recherche, publiés ou non, émanant des établissements d'enseignement et de recherche français ou étrangers, des laboratoires publics ou privés.



Distributed under a Creative Commons Attribution 4.0 International License

SCIENTIFIC REPORTS



OPEN

Molecular Dynamics Simulation of Water Confinement in Disordered Aluminosilicate Subnanopores

Takahiro Ohkubo¹, Stéphane Gin², Marie Collin² & Yasuhiko Iwadate¹

The porous structure and mass transport characteristics of disordered silicate porous media were investigated via a geometry based analysis of water confined in the pores. Disordered silicate porous media were constructed to mimic the dissolution behavior of an alkali aluminoborosilicate glass, i.e., soluble Na and B were removed from the bulk glass, and then water molecules and Na were introduced into the pores to provide a complex porous structure filled with water. This modelling approach revealed large surface areas of disordered porous media. In addition, a number of isolated water molecules were observed in the pores, despite accessible porous connectivity. As the fraction of mobile water was approximately 1%, the main water dynamics corresponded to vibrational motion in a confined space. This significantly reduced water mobility was due to strong hydrogen-bonding water-surface interactions resulting from the large surface area. This original approach provides a method for predicting the porous structure and water transport characteristics of disordered silicate porous media.

Water confined in the nanopores of silicate compounds has been widely studied to understand the specific structural and dynamical properties of such compounds. Silicate minerals and glasses are known to include water, and hydrolysis reactions can occur on the surface^{1–4}. However, predicting these reactions, which are important for mineral formation and carbon cycling related to CO₂ in air, is extremely complicated^{5,6}. In addition to natural minerals, confined water within artificial silicate materials, such as ordered silicates⁷ and synthetic clay minerals, is also attractive for chemical engineering applications⁸. In such confined spaces, water properties including its structure, melting point, and mobility differ significantly from those of bulk water^{9–11}. Consequently, theoretical and experimental methods have been employed to investigate the structural and dynamical properties of water confined in well-organized nanopores of varying sizes, geometries, and surface hydrophilic/hydrophobic features^{12–14}.

The properties of water in organized pores with one-dimensional tubes and two-dimensional nanosheets have been established using experimental and computational techniques. Various experimental techniques, including quasielastic neutron scattering (QENS)¹⁵, vibrational spectroscopy, and NMR have been used to investigate the properties of fluids in confined spaces^{16–19}. The translational and rotational dynamics of water are highly sensitive to size and surface charges. Reduced diffusion and rotational motion, two typical confinement effects, have been observed by QENS and ¹H NMR relaxation studies. Molecular dynamics (MD) simulations are also powerful in investigating the structure and dynamics of water in pores. MD simulations using cell sizes of 10 nm in length are now routinely used to gain insight into molecular behavior and mechanical properties. By constructing ideally shaped pores, the pore size and shape dependences of water properties have been systematically investigated and compared with experimental data^{12,20}. Although these MD studies have highlighted the importance of nanopore geometry, an understanding of water in nanopores with disordered shapes is still required.

For silicate glass systems, when soluble elements are released into solution by contact with water, the remaining silicate network forms a complicated porous structure filled with water²¹. Molecular modeling of this structure is extremely difficult owing to its complexity. Surfaces with a high fractal dimension are formed by hydrolysis and condensation reactions at water interfaces²², and the resultant structures are hardly predictable. Therefore, the water properties in simplified ordered pores are not applicable to understanding the confinement effects in such systems. Confined water in disordered silicate-water systems has only been discussed in a few MD simulations^{23–25}. Water in disordered calcium silicate hydrated gels shows slower diffusion than water in ordered pores²³.

¹Graduate School of Engineering, Chiba University, 1-33 Yayoi-cho Inage-ku, Chiba, 263-8522, Japan. ²CEA DEN DE2D SEVT, Laboratoire d'étude du Comportement à Long Terme, 30207, Bagnols-sur-Céze, France. Correspondence and requests for materials should be addressed to T.O. (email: ohkubo.takahiro@faculty.chiba-u.jp)

In this study, we modeled an aluminosilicate gel that might form by aqueous alternation of an alkali aluminoborosilicate glass. The glass, which has a composition of SiO_2 , B_2O_3 , Al_2O_3 , and Na_2O , is a typical engineering material used for electronic device displays, windows, and the immobilization of nuclear waste⁵. Simplified compositions have been studied to better understand corrosion mechanisms^{26–28}. The formation of altered layers on these glasses is attributed to the release of soluble elements, such as Na and B, into solution, followed by the re-polymerization of the silicate network²⁹. The random silicate networks of these glasses are necessary for their future performance and critical in designing their composition and manufacturing processes. For nuclear waste immobilization, the structure and transport properties of the altered layer on the glass surface is important for understanding the long-term performance when the glass is in contact with water⁵. Electron microscopy has revealed that nanoporous surface layers form during glass corrosion. When formed under silica-saturated conditions near neutral pH, these layers are passivating, and thus control the release of soluble elements from the glass^{30,31}.

A recent glass corrosion study revealed that the pore size of international standard glass (ISG) in silica-saturated solution at pH 7 is ≤ 1 nm³². The apparent diffusion coefficients of water on the order of 10^{-20} m²/s² were obtained from time-dependent elemental profiles within the surface layers³². This value is significantly lower than that for nanometer-scale ordered pores^{12–15}. The aim of this study was to investigate the regime between nanometer-scale ordered and disordered pores to provide insight into the porous structure and dynamics of water confined in disordered spaces.

Computational Method

To construct a model of disordered aluminosilicate gels, four steps were used that followed realistic phenomena during borosilicate glass dissolution. First, a bulk glass model was made with the desired composition; second, soluble elements were removed from the bulk glass; third, Si was substituted with Al and water molecules and Na^+ were introduced to match previously obtained experimental results³²; finally, the system was equilibrated. Al substitution for Si in the third step permits comparison with available experimental data. Details are described later in this section. A well-organized three-body potential function was used for the first step. The second and third steps were continuously performed using the final structure from the first step. Finally, a MD simulation with ClayFF force fields was conducted using the structure obtained from the third step. All MD simulations were performed using LAMMPS code³³. Detailed descriptions of each step are given below.

Bulk glass with an experimental density of 2.5 g/cm³ was constructed with a composition of 67.8SiO₂-18.0B₂O₃-14.2Na₂O and 3004 atoms (Si: 606, B: 322, Na: 254, O: 1822). This molar ratio and density match those of ISG⁵. The potential function for the MD simulations of the bulk glass used Born-Mayer-Huggins (BMH) potential parameters. An additional three-body potential was used for the O-Si-O, O-B-O, and Si-O-Si angles. The two- and three-potential parameters, taken from references^{34,35}, were developed to reproduce first-neighbor distances and the B coordination number. Glass construction was performed by a melt-quenching process. The 3004 atoms were randomly distributed in the cell. The initial structure was melted at 3000 K for 100 ps, and then the temperature was decreased to 1773 K at 12.27 K/ps. After reaching energy equilibrium during a 100 ps run at 1773 K, a solid glass was prepared at 300 K by quenching the molten glass from 1773 to 300 K at 14.73 K/ps. All bulk glass simulations were performed in the NVT ensemble (constant number of particles, constant volume, and constant temperature)^{36,37}. The final glass structure comprised tetrahedral Si with four coordination sites and three- and four-coordinated B.

In the second step, B and Na, as soluble elements in the glass, were removed to create a disordered silicate network. Free O atoms resulting from a lack of B were also removed, and nonbridging O atoms were terminated with H.

The third step involved the substitution of Si with Al and the introduction of water molecules into the molecular model obtained from the second step. The atomic composition was matched to the experimentally observed surface layer of ISG glass after dissolution for 209 days at 90 °C³². The altered layer contained Al. Therefore, 67Si was randomly replaced with Al to match the experimental data; the replacement of SiO₄ tetrahedra bonded to substituted AlO₄ tetrahedra was avoided according to the Al-O-Al avoidance rule suggested by Loewenstein³⁸. H₂O, H₃O⁺, and Na were also randomly introduced into the void space, avoiding overlap with other atoms. This operation was performed with an atomic distance threshold of at least 2.0 Å to avoid unphysical interactions and structural breakage at the beginning of the simulations. The number of Na⁺ in the gels was 28, as determined from the concentration profile of Na in the altered layer³². A small amount of Na absorbed in the altered layer was also reported by solid-state NMR spectroscopy³⁹.

We targeted three disordered silicate gels with different water contents (5.4, 18.1, and 31.3 wt%). Recently, the water molecule content of altered layers on ISG glass at pH 7 and 90 °C was estimated by thermal gravimetric analysis (total water content) and ¹H NMR (water speciation). The determined value of 8 wt% falls within the range studied here²⁹. Substitution of Si with Al caused the system to be negatively charged; therefore, the excess negative charge was compensated by Na⁺ and the introduction of H₃O⁺ instead of H₂O. The number of molecules and atoms in these systems are summarized in Table 1.

MD simulations were performed for the three models using the ClayFF force field⁴⁰. The original ClayFF potential parameters cause a charge unbalance when hydroxyl oxygens are bonded to Al. Modified ClayFF potential parameters were developed by Kerisit *et al.*⁴¹; these predict contact between the silicate structure and water on the surface. Interatomic interactions were modeled with the SPC/E water model⁴². The potential model of Kusaka *et al.* used to model H₃O⁺ was developed by fitting the potential parameters for the interaction of the hydronium ion with H₂O to the experimental enthalpy of hydration for up to six water molecules⁴³. The validity of this model was also confirmed by Kerisit *et al.*⁴¹. The geometries of H₂O and H₃O⁺ were treated as rigid using the SHAKE algorithm⁴⁴. All potential parameters are listed in Tables S1–S4 in the Supplementary information.

All gel simulations were performed in the NPT ensemble (constant number of particles, constant pressure, and constant temperature) at 300 K and 1 atm^{36,37,45}. The temperature was held constant by using the Nosé-Hoover

	Si	Al	H ₂ O	H ₃ O ⁺	Na	O	OH	Volume Å ³
wc05	537	67	100	39	28	350	830	39079
wc18	529	67	500	39	28	328	846	47012
wc31	508	67	1050	39	28	296	898	63574

Table 1. Number of atoms and molecules in disordered gels with water contents of 5.4% (wc05), 18.1% (wc18), and 31.2% (wc31). The average box sizes are also listed.

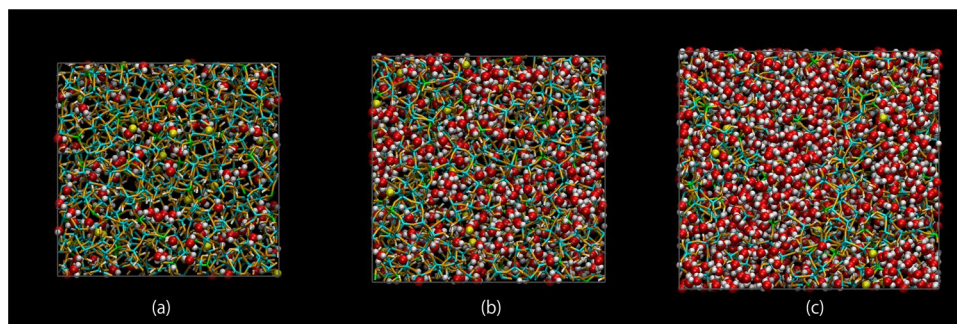


Figure 1. Atomic configurations of wc05 (a), wc18 (b), and wc31 (c). Cyan, lime, orange, and ivory bars correspond to Si, Al, O, and H, respectively, in the frameworks of the gels. Yellow, red, and white balls indicate Na, O, and H, respectively, of water and hydronium. Average side lengths of wc05, wc18, and wc31 are (34.537,33.169234.113), (36.389,35.2147,36.687), and (40.546,36.998,42.379) in Å, respectively. All angles of the unit cells are 90 degree.

thermostat⁴⁶. The electrostatic interactions were calculated using the particle-particle-particle mesh method⁴⁷ with a relative error of 0.0001 Kcal/mol/Å in the force and a real-space cutoff of 9 Å. The same cutoff was used for short-range interactions. For the initial structure, the atom trajectories were generated by the Verlet algorithm for 5000 steps with a time step of 0.001 fs. The time step was gradually increased to 0.001, 0.01, and 0.1 fs with each run of 5000 steps. A time step of 1 fs was finally employed for long simulation runs.

This simulation procedure produced unrealistic Si coordination numbers (CN = 2 and 3) owing to volume expansion in the initial simulation periods. We removed these unrealistic Si and Al units and the resultant free O, whereas the nonbridging O atoms generated by this treatment were terminated with H. After this treatment, the simulation was restarted from the new structure with a time step of 1 fs. This operation was repeated until unrealistic Si and Al coordination numbers were not formed during long simulations, that is, all Si and Al had four-coordinated tetrahedral structures and all nonbridging O atoms were hydroxyl oxygens. The final compositions of Si and O are listed in Table 1. After energy equilibrium was reached (~50 ns), a MD simulation for sampling atomic configurations was performed for 10⁹ steps (1 μs). The sampled atomic configurations were analyzed to understand the structural and dynamical properties.

Static structures were also generated by decreasing the temperature to 1 K with a time step of 1 fs in the NVT ensemble (constant number of particles, constant volume, and constant temperature) after a 1 μs simulation run under the average cell size of an NPT run. After 50000 steps at 1 K, the final atomic configurations were used for structural analysis of the pores based on the Voronoi network using Zeo++⁴⁸.

For comparison, MD simulations of bulk water comprising 512 H₂O molecules were performed using the same water potential parameters as for the aluminosilicate gel.

Results and Discussion

Structural properties. The structural properties of the three gels were investigated from the perspective of porous spaces and water structures. Here, the pores were defined as the volumes not occupied by framework atoms (Si, Al, and O). Pore analyses were performed on the static structures described in the Computational Methods section.

Voronoi-based surface reconstruction was used to define the boundary between pores and the volume occupied by the framework atoms, which was calculated from the finite atomic sizes of Si, Al, and O. Atomic sizes corresponding to the covalent radii were employed to define the atomic volumes. We used 1.16, 1.26, and 0.63 Å for Si, Al, and O, respectively⁴⁹. Structural analyses of the pores were performed by determining the pore volumes, surface areas, and pore size distributions. Radial distribution functions and the cluster size distributions of water were estimated to understand the local structure and connectivity of water in confined spaces.

Figure 1 shows a visualization of the atoms and bonds in wc05, wc18, and wc31 at the final step. Atomic configurations and cell parameters are also provided in the Supplementary information in CIF format. Protons on hydroxyl groups are oriented towards O on water or hydronium molecules in the pores, suggesting the formation of OH-water hydrogen bonds. Population of hydrogen bonded water with surface hydroxyl hydrogen or bridging oxygen was estimated for all water and hydronium. We used the H-O cutoff distance of 2.0 Å corresponding to

	Density (g/cm ³)	Si					Al				
		Q ⁰	Q ¹	Q ²	Q ³	Q ⁴	Q ⁰	Q ¹	Q ²	Q ³	Q ⁴
wc05	1.993	2.2	11.5	27.4	38.9	19.9	0.0	10.4	35.8	35.8	17.9
wc18	1.898	2.3	11.5	28.9	38.8	18.5	1.5	14.9	35.8	32.8	14.9
wc31	1.640	2.6	14.6	31.1	37.0	14.8	1.5	19.4	43.3	28.4	7.5

Table 2. Densities and populations (%) of Si- and Al-Qⁿ species in wc03, wc18, and wc31.

	V (Å ³)	AV (Å ³)	NAV (Å ³)	SA (Å ²)	NSA (Å ²)	P (%)	D (Å)	F (%)	SSA (m ² /g)
wc05	39079	399	5.47	1240	89.2	10.2	1.29	70	1710
wc18	47012	1020	0.940	1830	17.3	21.8	2.24	100	2540
wc31	63574	2570	2.86	2260	25.9	40.5	4.56	100	3200

Table 3. Total volume (V) and characteristic parameters of the space, excluding framework atoms in the cell. AV: accessible volume; NAV: inaccessible volume; SA: accessible surface area; NSA: inaccessible surface area. Porosity (P) and diameter (D) were calculated as $100 \times AV/V$ and $4 \times AV/SA$, respectively. Fraction of AV filled with water (F) was estimated from the structure with water present. Specific surface area (SSA) corresponds to SA per mass of framework atoms.

hydrogen-bond formation. The time-averaged populations of hydrogen bonded water in wc05, wc18, and wc31 were 98.8, 92.7, and 74.1%, respectively. Most of water molecules in wc05 and wc18 have hydrogen bonding to atoms on the pore surface. The shapes of the water-filled pores are highly complex compared to those previously reported in MD studies of ordered silicate materials including water^{12–14}. Vacant pores without water molecules and a few isolated water molecules were also identified in wc05. These water molecules were trapped in small spaces formed within the aluminosilicate network. Confined water molecules in disordered silicate channels were previously modeled from layered calcium silicate hydrate (CSH) by MD simulations at an unrealistically high temperature (1500 K)²³. However, the degree of disorder in the modeled CSH structure is much lower than that in this study. For example, the layered channel structure of water-filled pores was retained, even when the silicate structure was destroyed by high-temperature annealing. In comparison, the building steps described in the computational method are suitable for modeling highly complex gels.

The Si and Al populations in bridging Qⁿ structures (*n* is the number of bridging O) and the densities of wc05, wc18, and wc31 are shown in Table 2. Different Qⁿ species with different water contents arise from the elimination of unrealistic Si units formed by volume expansion during the initial NPT MD runs. The eliminated numbers of Si were 69, 77, and 98 for wc05, wc18, and wc31, respectively, corresponding to 11, 13, and 16% of the 606 Si in the bulk glass. Thus, the extents of the disordered silicate network and the bulk glass structure were nearly equal. The density, which was calculated from the average volume during the simulation run, was decreased with increasing water content, indicating that volume expansion was caused by introducing excess water.

Accessible and inaccessible pore volumes were evaluated by the Monte Carlo approach with a probe molecule using Zeo++⁴⁸. In these analyses, a random position in the cell was chosen, and the position was checked to determine whether the probe molecule overlapped with the framework atoms. We used a probe molecule size of 1.41 Å, corresponding to the mean van der Waals radius of water molecules assigned from the Bjerrum four-point charge model for water⁵⁰. If the probe molecule did not overlap the framework atoms, the space was considered a pore. This procedure was iterated until convergence; 100,000 iterations permitted estimation to three significant figures within 1% error. Furthermore, the identified pores were classified as accessible or inaccessible volumes based on whether the pores could connect with each other or were isolated, respectively. The pore connections were considered under periodic conditions, that is, connections between pores at edge positions in the simulation box and pores at the opposite side were estimated. The fraction of the accessible volume filled with water was estimated with the same procedure, where water was approximated as a sphere with a radius of 1.41 Å.

The surface area of the probe molecule is also a characteristic parameter that can be used to understand pore geometry, which is directly related to surface interactions between framework atoms and water molecules. In addition to the accessible and inaccessible pore volumes, the accessible and inaccessible surface areas were calculated using probe molecules with a size of 1.41 Å using Zeo++⁴⁸.

The accessible and inaccessible pore volumes (AV and NAV) and accessible and inaccessible surface areas (SA and NSA) for wc05, wc18, and wc31 are listed in Table 3. The specific surface area (SSA) was calculated from the SA and the mass of framework atoms. The total accessible pore volume is increased with increasing water content because the unit cell expands in the presence of excess water molecules. The accessible volume of 70% in wc05 corresponds to vacant pores without water. The detected pore volumes of wc05, wc18, and wc31 mainly comprise accessible volume, indicating that small channels connect the pores. The porosity (%) was also estimated by dividing the pore volume by the total volume. Average pore diameters were calculated based on the accessible volume and the surface area by assuming cylindrically shaped pores with diameters proportional to the surface-to-volume ratio ($4 \times AV/SA$).

The obtained porosities and average pore diameters were compared with those of ordered porous materials, such as two-dimensional clay sheets and one-dimensional MCM-41. For a typical clay sheet, the thicknesses of a hydrated layer and the framework layer are 3.2 and 9.2 Å, respectively⁵¹. From this geometry, the porosity and

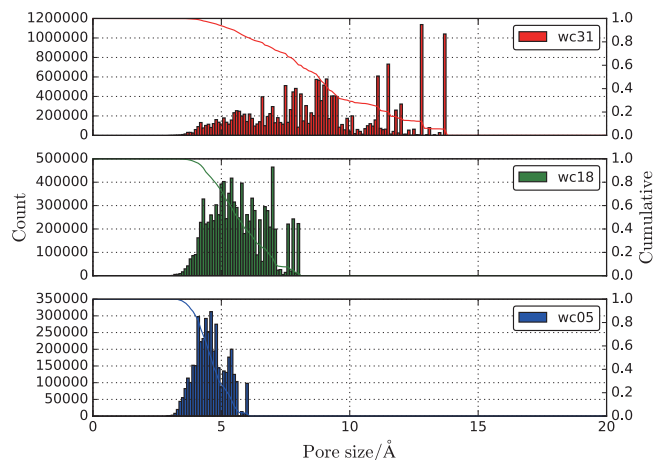


Figure 2. Pore size distribution of count on left axis and cumulation on right axis of wc05, wc18, and wc31. Pores are defined as the spaces not occupied by the gel framework (Si, Al, O, and OH).

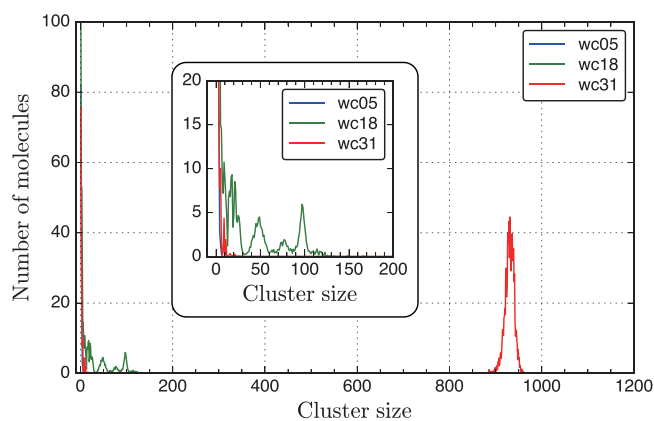


Figure 3. Cluster size distributions of water in wc05, wc18, and wc31 with a cutoff distance of 3.05 Å. The vertical axis shows the number of molecules with a given cluster size. The inset shows the distribution of small cluster sizes ranging from 0 to 200.

pore diameter ($4 \times AV/SA$) with two hydrated layers in the clay sheet are 59% and 12.8 Å, respectively, which are higher than those of the modeled structure in this study. Unlike hydrated clays, MCM-41 is a typical ordered material with one-dimensional pores that range in size from 20 to 100 Å⁵², one to two orders of magnitude larger than those in this study. According to the International Union of Pure and Applied Chemistry (IUPAC) system⁵³, pores with sizes below 25 Å are classified as micropores. Unfortunately, few systematic studies have analyzed porous materials with pore sizes of approximately 10 Å. To our best knowledge, this study is the first to model highly complex porous materials to characterize structure and confined water.

Pore size distributions in the accessible volume were also calculated to understand the porous structure. Further, a position in the accessible volume was randomly chosen and analyzed to find the largest encapsulating sphere without framework atoms. The choice of the random position was iterated, the largest encapsulating sphere was stored, and any overlap with other encapsulating spheres was detected. We confirmed that 50000 and 100000 iterations yielded the same pore size distribution profiles. The pore size distributions and cumulation in wc05, wc18, and wc31 are displayed in Fig. 2. A Gaussian-like distribution centered at a pore size of 4 Å is identified in wc05. Higher counts on the larger pore size side are observed at around 8 and 13 Å in wc18 and wc31, respectively. This trend suggests that water molecules aggregate to form water channels that ease transport. To directly estimate water aggregation, the cluster size distribution is calculated.

To characterize the connectivity of water-filled pores, we calculated the cluster size distribution of water (Fig. 3), where a cluster was defined as the number of connected water molecules under periodic conditions. For example, if three water molecules were connected within the cutoff distance, the cluster size was 3. The cluster size distribution is indicated by a histogram of the number of water molecules; that is, for four clusters with cluster size 3, the height of the cluster size 3 is 12 in the histogram. We determined the cutoff distance of 3.05 Å from the O-O distance of the first peak in the H₂O-H₂O radial distribution functions (Fig. 4), which roughly includes all water molecules in the first hydration shell. The time-averaged cluster size was obtained from all configurations during the simulation period.

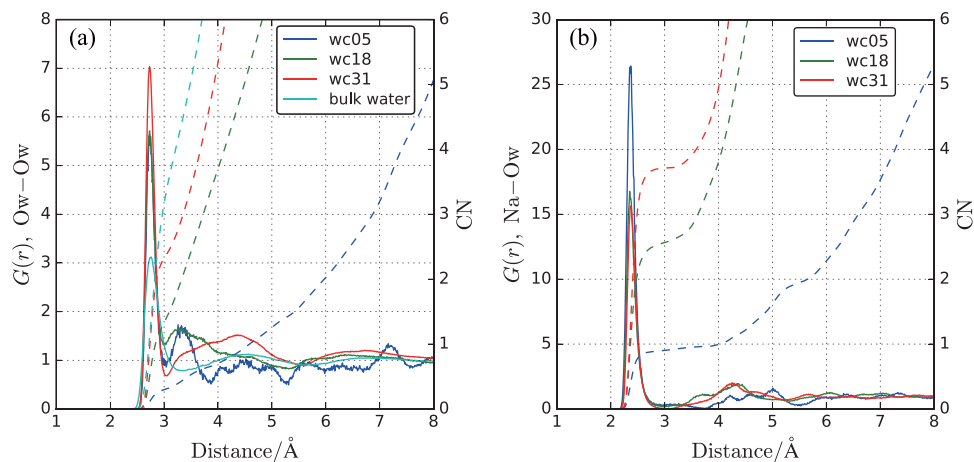


Figure 4. Radial distribution functions $G(r)$ (solid lines, left axis) and running coordination number, CN (dashed lines, right axis) of wc05, wc18, and wc31. (a) The Ow (H₂O)–Ow (H₂O); (b) Na–Ow (H₂O). The Ow (H₂O)–Ow (H₂O) $G(r)$ of bulk water is also shown in the left figure for comparison.

All cluster sizes observed for wc05 were less than 10. Several peaks corresponding to cluster sizes of 0–150 were observed for wc18. These peaks with higher cluster sizes are consistent with the pore size distributions shown in Fig. 2. Many water molecules belong to small cluster sizes of less than 10. By combining the information in Figs 2 and 3, we can describe the morphology of the water network in hydrated gels. At low water content (wc05), there are many small isolated water clusters and vacant pores. At higher water contents (wc18 and wc31), a few large water clusters govern the water distribution. However, the cluster size distribution is significantly inhomogeneous.

The local structure of confined water in the gel is investigated using the radial distribution functions, $G(r)$, between water O atoms (Fig. 4(a)). For comparison, the corresponding $G(r)$ of bulk water obtained from the SPC/E water model⁴² is also displayed. The O–O distances of the first peak in wc05, wc18, and wc31 (2.73–2.74 Å) are independent of water content. The first minimum at 3.05 Å is used as the cutoff for estimating the cluster size distribution in Fig. 3. The position of the first peak of bulk water is 2.76 Å, similar to that calculated from another potential model of bulk water⁴⁸. Although the O–O distance of confined water is slightly shorter than that of bulk water, the confinement effect on the water–water distance is not significant. However, clear second peaks are observed at approximately 3.3 Å in wc05 and wc18, and 4.4 Å in wc31, which are not confirmed in bulk water. The position of the second peak in wc31 is almost identical to that of bulk water, indicating that the aggregated structure of water in relatively large clusters is similar to that of bulk water. The shorter distance of the second peaks in wc05 and wc18 suggests closely packed water clusters in the pores. As the water content increases, this second peak is weakened and almost disappears in wc31. The peak positions are consistent with those for water in Nafion membranes with 5% water content, which are solid polymer materials showing high water diffusivity^{54–56}.

The coordination number of water molecules attached to other water molecules is increased with increasing water content, approaching that of bulk water. The coordination number of 4 observed in bulk water at 3.22 Å is not allowed in wc05 and wc18. These small coordination numbers are influenced by geometrical effects caused by the large surface areas and small volumes in confined pores. The coordination structure of water around Na is depicted in Fig. 4(b). The Na⁺–H₂O O distances and coordination numbers in Na aqueous solution, determined experimentally and by MD simulation, are 2.29–2.40 Å and 4.3–6.2, respectively^{57–60}. The coordination number of water around Na⁺ calculated for the first coordination sphere at 3 Å increases with increasing water content (0.903, 2.56, and 3.71). In contrast, the Na⁺–H₂O O distance is not influenced by water content (2.35–2.37 Å) and agrees with the value in bulk Na aqueous solution. Structural changes of Na⁺ solvation in a confined space affect the coordination number rather than the coordination distance.

Dynamical properties of water. The dynamical properties of water in the gels were evaluated through the square displacements and van Hove functions of water molecules.

The square displacement (SD) of an individual water molecule is defined as

$$SD_i(t) = |r_i(t) - r_i(0)|^2 \quad (1)$$

where $r_i(t)$ is the position of each O atom i in water at time t . The examples of three water molecules in wc18 are shown in Fig. 5. Water corresponding to the blue and green lines is relatively less displaced and can be considered “immobile water”. In comparison, water corresponding to the red line experiences hopping at 0.6 μs, and can be considered “mobile water”. The distinction between mobile and immobile water molecules is based on the histogram of the standard deviation of the SD, as shown in Fig. 6. Most water molecules have deviations of 0.1 and 0.2, independent of the water content, mainly because water molecules move freely in the confined spaces formed by neighboring water molecules and the surface of the aluminosilicate network. A small gap is observed at a standard deviation of 0.8 Å² in the inset of Fig. 6. As shown in Fig. 5, standard deviations above 0.8 Å² correspond to hopping water molecules in the simulation period (1 μs). Therefore, we used a standard deviation of 0.8 Å² to

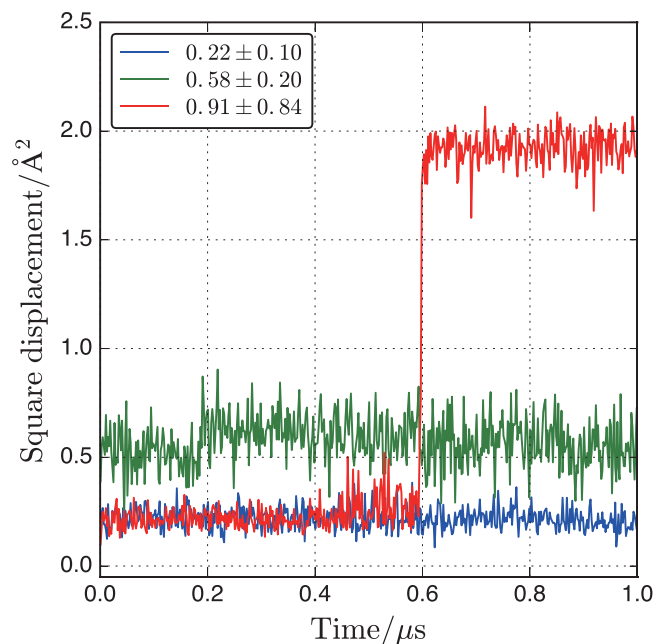


Figure 5. Typical square displacement behavior of three water molecules in wc18. The values in the legend indicate the averages and standard deviations.

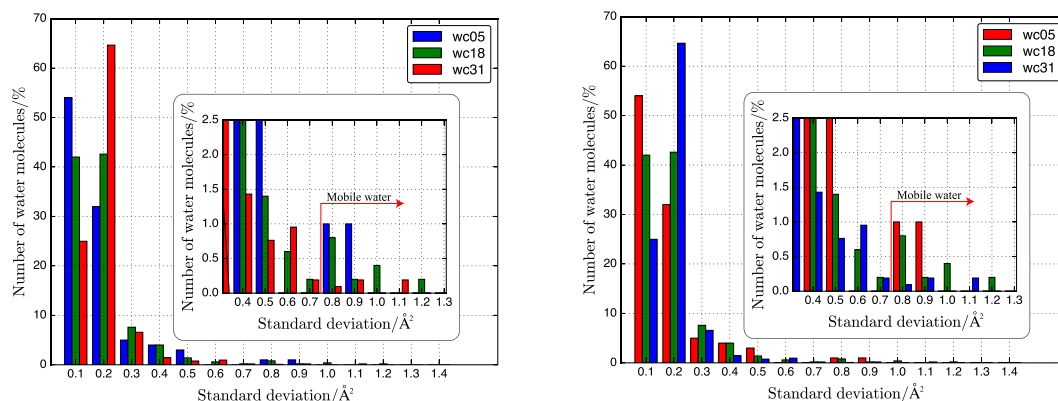


Figure 6. Histogram of standard deviations for square displacement of water molecules in wc05, wc18, and wc31. The inset shows expanded data ranging from 0.3 to 1.3 Å².

distinguish mobile and immobile water. The fractions of mobile water are 1.0, 0.8, and 0.4% for wc05, wc18, and wc31, respectively. The higher fraction of mobile water in wc05 suggests that water can hop into a vacant pore via a stochastic process. However, these mobile water molecules are not a major component.

The mean square displacement (MSD) of H₂O in wc05, wc18, and wc31 is calculated from the SD averaged over the total number of water molecules (Fig. 7):

$$\text{MSD}(t) = \frac{1}{N} \sum_{i=1}^N |r_i(t) - r_i(0)|^2. \quad (2)$$

A nonlinear increase of MSD is observed for wc18. However, the MSD of water in wc05 frequently shows singular jumps with an interval of approximately 0.2 μs. This behavior suggests that there is frequent cooperation between hopping water molecules. For wc18, water molecules only move ballistically up to 0.6 μs, $\propto t^2$. Similar behavior has been reported for water in calcium-silicate-hydrate and on amorphous silica surfaces^{24,61}. Step-like increases of water are also confirmed in wc31, but the plateau and slope period is approximately 0.2 μs, which is shorter than that in wc18. Thus, the behavior of the MSD is close to the Einstein relation ($\propto t$) observed in liquids.

To improve the MSD statistics, time averaging of $\langle \text{MSD} \rangle$ during $t = 500$ ns at multiple time origins ($r_i(0)$) with 5 ns time shifts was performed for wc31. Self-diffusion coefficients can immediately be calculated from the Einstein relation, $D = \text{MSD}/6t$, for a linear region at long times (250 ns period). Unfortunately, the $\langle \text{MSD} \rangle$ of water in wc05 and wc18 were not linear functions of time, indicating that the simulation period was insufficient

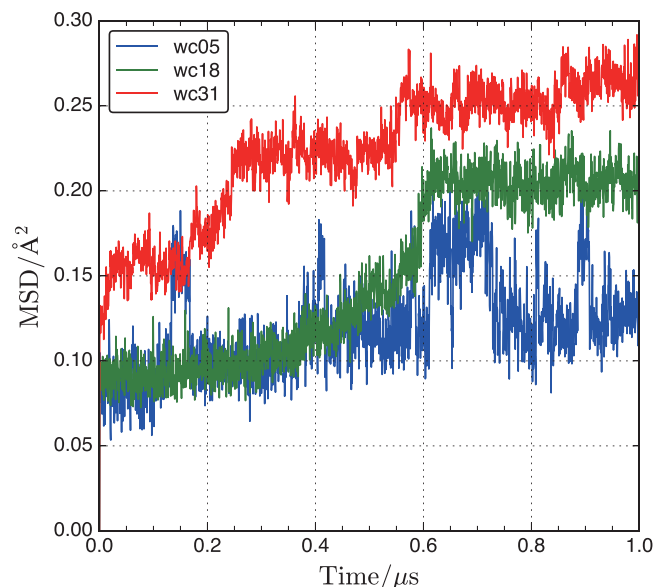


Figure 7. Mean square displacement of water in wc05, wc18, and wc31.

to estimate D . The D value for water in wc31 is $8 \times 10^{-16} \text{ m}^2/\text{s}$, which is extremely small compared to the reported D values for water in ordered silicate materials such as clay sheets and MCM-41^{12,20}. Tortuous diffusion paths arising from the disordered porous structure rather than the straight diffusion paths in ordered silicate materials affect the D value considerably.

MD simulations of silica nanopores with various pore sizes revealed that the confinement effect of D for water gradually decreases for pore sizes less than 5 \AA ^{12,13}. This trend is inconsistent with the result of this study; that is, the translation of water is dramatically limited regardless of the pore size. Possible reasons for this difference include the geometry of the diffusion path and the large surface area arising from the complex pore shapes. Interactions between OH on the pore surface and water effectively suppress water displacement and form hydrogen bonds between water and OH. Complex pore shapes with large surface areas thus allow the development of more hydrogen bonds than ordered pore shapes. Although the space is classified as accessible (Table 3), large surface areas for forming hydrogen bonds limit the accessibility of any space. The rotational correlation function of water, $C(t)$, which is an index of hydrogen bonds, is defined as follows:

$$C(t) = \frac{1}{2N} \sum_i^N (3[\cos^2\theta(\tau)] - 1) = \frac{1}{2N} \sum_i^N (3[d_i(\tau) \cdot d_i(0)]^2 - 1) \quad (3)$$

where $d_i(\tau)$ is the dipole axis vector of water molecule i . We calculated $C(t)$ for water molecules during the simulation run. $C(t)$ for wc05, wc18, and wc31 are shown in Fig. S1 in the Supplementary information. The rotational dynamics of water molecules were clearly restricted by the developed hydrogen bonds.

Experimentally, D for water was observed from the elemental profile of H in an altered layer on a glass surface after glass dissolution in water³². The D value of $8 \times 10^{-20} \text{ m}^2/\text{s}$ was four orders of magnitude less than the diffusivity in wc31. It is worth noting that water diffusivity is strongly influenced by the water content; i.e., the water content is probably lower than that in wc31³², which causes strong interactions with the solid surface because of the small cluster size. Thus, water molecules are confined in a sub-nanometer space with ultra-low diffusivity.

The van Hove correlation function ($H(r, t)$), which is a better expression for understanding water hopping in pores, is defined as follows:

$$H(r, t) = \frac{1}{N} \sum_i^N \langle \delta(r - |r_i(t + \tau) - r_i(\tau)|) \rangle \quad (4)$$

where r_i is the coordinates of oxygen atom i in water, δ denotes the Kronecker function, and the brackets represent time averaging at multiple time origins, τ . We calculated $H(r, t)$ for water molecules at $t = 500 \text{ ns}$. $H(r, t)$ for mobile and immobile water in wc05, wc18, and wc31 are shown in Fig. 8. The peak centered at 0.2 \AA in $H(r, t)$ for immobile water in wc05, wc18, and wc31 corresponds to vibrational motion in a confined space. However, mobile water mainly shows two peaks at approximately 0.3 and 2 \AA . The latter distance implies escape from a cage-like confined space, which corresponds to the apparent pore size for water diffusion. This distance cannot be clearly differentiated from the pore size distribution shown in Fig. 2. Therefore, the diffusion energy barrier for transition from the immobile to the mobile state is governed by surface interactions rather than pore geometry. This concept can be used to understand ultra-confined water in disordered pores.

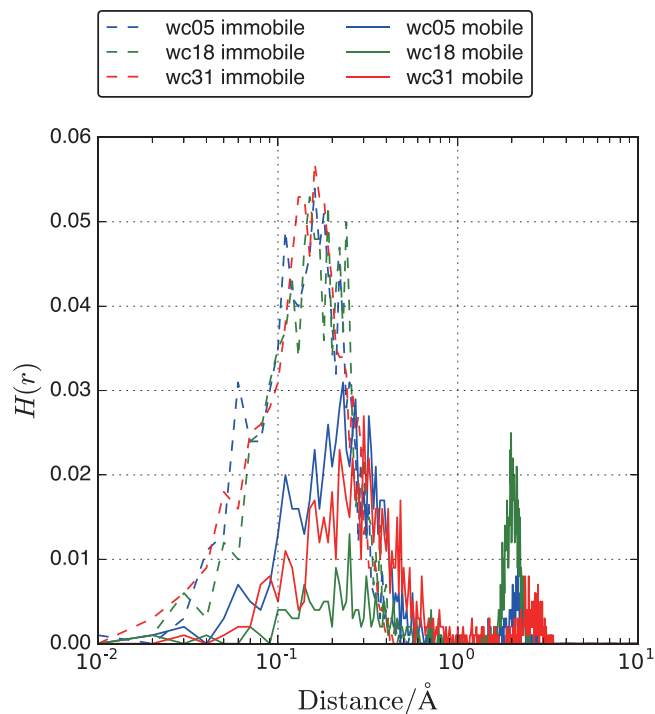


Figure 8. Van Hove function at $t = 500$ ns for immobile (dashed) and mobile (solid) water in wc05, wc18, and wc31.

Conclusions

Various gels formed by glass dissolution were carefully studied using the MD method for long periods of $1 \mu\text{s}$. The molecular structures of aluminosilicate porous gels including water were modeled from borosilicate glass by removing soluble elements, mimicking the chemical processes of glass alteration following contact with water. The aluminosilicate porous network comprised four-coordinated Si and Al tetrahedra with nonbridging O terminated with H. Three water contents (5, 13, and 31%) were considered to understand the structures and dynamics of confined water.

Structural analyses of porous structures were carried out by examining accessible and inaccessible volumes and surface areas using a probe molecule (1.41 \AA diameter). The pores were classified as accessible, with sub-nanometer sizes and extremely large surface areas compared to those of ordered silicate materials. Local structures of water and Na^+ revealed unusually low coordination numbers for confined water. Cluster sizes, corresponding to the connectivity of the water channels, were dramatically increased with increasing water content. Indeed, water channels were identified in snapshots of the materials with 31% water content.

The mobility of water molecules was extremely limited, despite the formation of water clusters. Mobile and immobile water molecules were identified based on the square displacement of water for $1 \mu\text{s}$. The amount of water experiencing hopping events was less than 1%, regardless of the water content. The mean hopping distance of water molecules was around 2 \AA , as determined from the van Hove function. Importantly, this hopping distance was independent of the water content. Although the pores were classified as accessible and water formed clusters as transport channels, strong interactions between water and neighboring atoms suppressed water mobility. This feature is characteristic of disordered aluminosilicate gels with large surface areas.

Overall, this work targeted the equilibrium state of water in ultra-confined disordered aluminosilicate networks. As proton association-dissociation of the surface hydroxyl groups is an important reaction for the formation of aluminosilicate networks, we will focus on the kinetics of this process in our future work.

References

- Hellmann, R. *et al.* Unifying natural and laboratory chemical weathering with interfacial dissolution–reprecipitation: A study based on the nanometer-scale chemistry of fluid–silicate interfaces. *Chem. Geol.* **294**, 203–216 (2012).
- Hellmann, R. *et al.* Nanometre-scale evidence for interfacial dissolution–reprecipitation control of silicate glass corrosion. *Nat. Mater.* **14**, 307–311 (2015).
- Ruiz-Agudo, E., Putnis, C. V., Rodriguez-Navarro, C. & Putnis, A. Mechanism of leached layer formation during chemical weathering of silicate minerals. *Geology* **40**, 947–950 (2012).
- Daval, D., Hellmann, R., Saldi, G., Wirth, R. & Knauss, K. Linking nm-scale measurements of silicate surfaces to macroscopic dissolution rate laws: New insights based on diopside. *Geochim. Cosmochim. Acta* **107**, 121–134 (2013).
- Gin, S. *et al.* An international initiative on long-term behavior of high-level nuclear waste glass. *Mater. Today* **16**, 243–248 (2013).
- Sissmann, O. *et al.* Enhanced olivine carbonation within a basalt as compared to single-phase experiments: Reevaluating the potential of CO_2 mineral sequestration. *Environ. Sci. Technol.* **48**, 5512–5519 (2014).
- Li, W. & Zhao, D. An overview of the synthesis of ordered mesoporous materials. *Chem. Commun.* **49**, 943–946 (2013).

8. Liu, C., Qu, Y., Luo, Y. & Fang, N. Recent advances in single-molecule detection on micro- and nano-fluidic devices. *Electrophoresis* **32**, 3308–3318 (2011).
9. Kittaka, S., Ishimaru, S., Kuranishi, M., Matsuda, T. & Yamaguchi, T. Enthalpy and interfacial free energy changes of water capillary condensed in mesoporous silica, mcm-41 and sba-15. *Phys. Chem. Chem. Phys.* **8**, 3223–3231 (2006).
10. Jähner, S. *et al.* Melting and freezing of water in cylindrical silica nanopores. *Phys. Chem. Chem. Phys.* **10**, 6039–6051 (2008).
11. Deschamps, J., Audonnet, F., Brodie-Linder, N., Schoeffel, M. & Alba-Simionesco, C. A thermodynamic limit of the melting/freezing processes of water under strongly hydrophobic nanoscopic confinement. *Phys. Chem. Chem. Phys.* **12**, 1440–1443 (2010).
12. Bourg, I. C. & Steefel, C. I. Molecular dynamics simulations of water structure and diffusion in silica nanopores. *J. Phys. Chem. C* **116**, 11556–11564 (2012).
13. Renou, R., Szymczyk, A. & Ghoufi, A. Water confinement in nanoporous silica materials. *J. Chem. Phys.* **140**, 044704 (2014).
14. Milischuk, A. A. & Ladanyi, B. M. Structure and dynamics of water confined in silica nanopores. *J. Chem. Phys.* **135**, 174709 (2011).
15. Briman, I. M. *et al.* Impact of pore size and pore surface composition on the dynamics of confined water in highly ordered porous silica. *J. Phys. Chem. C* **116**, 7021–7028 (2012).
16. Sahasrabudhe, A., Mitra, S., Tripathi, A., Mukhopadhyay, R. & Gupta, N. Effect of pore characteristics on the dynamics of cyclohexane molecules confined in zsm-5 and mcm-41 molecular sieves: Ftir and qens study. *Phys. Chem. Chem. Phys.* **5**, 3066–3075 (2003).
17. Faraone, A. *et al.* Translational and rotational dynamics of water in mesoporous silica materials: Mcm-41-s and mcm-48-s. *J. Chem. Phys.* **119**, 3963–3971 (2003).
18. Takahara, S., Sumiyama, N., Kittaka, S., Yamaguchi, T. & Bellissent-Funel, M.-C. Neutron scattering study on dynamics of water molecules in mcm-41. 2. determination of translational diffusion coefficient. *J. Phys. Chem. B* **109**, 11231–11239 (2005).
19. Schmidt, R., Hansen, E. W., Stoecker, M., Akporiaye, D. & Ellestad, O. H. Pore size determination of mcm-41 mesoporous materials by means of 1h nmr spectroscopy, N₂ adsorption, and hrem. a preliminary study. *J. Am. Chem. Soc.* **117**, 4049–4056 (1995).
20. Holmboe, M. & Bourg, I. C. Molecular dynamics simulations of water and sodium diffusion in smectite interlayer nanopores as a function of pore size and temperature. *J. Phys. Chem. C* **118**, 1001–1013 (2013).
21. Gin, S. *et al.* Nuclear glass durability: New insight into alteration layer properties. *J. Phys. Chem. C* **115**, 18696–18706 (2011).
22. Caillateau, C., Devreux, F., Spalla, O., Angeli, F. & Gin, S. Why do certain glasses with a high dissolution rate undergo a low degree of corrosion? *J. Phys. Chem. C* **115**, 5846–5855 (2011).
23. Hou, D., Li, D., Zhao, T. & Li, Z. Confined water dissociation in disordered silicate nanometer-channels at elevated temperatures: Mechanism, dynamics and impact on substrates. *Langmuir* **32**, 4153–4168 (2016).
24. Qomi, M. J. A., Bauchy, M., Ulm, F.-J. & Pellenq, R. J.-M. Anomalous composition-dependent dynamics of nanoconfined water in the interlayer of disordered calcium-silicates. *J. Chem. Phys.* **140**, 054515 (2014).
25. Hlushkou, D., Svidrytski, A. & Tallarek, U. Tracer-size-dependent pore space accessibility and long-time diffusion coefficient in amorphous, mesoporous silica. *J. Phys. Chem. C* **121**, 8416–8426 (2017).
26. Hopf, J. *et al.* Glass–water interaction: Effect of high-valence cations on glass structure and chemical durability. *Geochim. Cosmochim. Acta* **181**, 54–71 (2016).
27. Angeli, F., Charpentier, T., Gaillard, M. & Jollivet, P. Influence of zirconium on the structure of pristine and leached soda-lime borosilicate glasses: Towards a quantitative approach by ¹⁷O MQMAS NMR. *J. Non-Cryst. Solids* **354**, 3713–3722 (2008).
28. Pierce, E. M. *et al.* Experimental determination of the effect of the ratio of b/al on glass dissolution along the nepheline (NaAlSiO₄)–malinkoite (NaBSiO₄) join. *Geochim. Cosmochim. Acta* **74**, 2634–2654 (2010).
29. Collin, M. *et al.* Structure of international simple glass and properties of passivating layer formed in circumneutral pH conditions. *npj-Materials Degradation* **2**, 4 (2018).
30. Gin, S. *et al.* Atom-probe tomography, tem and tof-sims study of borosilicate glass alteration rim: A multiscale approach to investigating rate-limiting mechanisms. *Geochim. Cosmochim. Acta* **202**, 57–76 (2017).
31. Putnis, A. Glass corrosion: Sharpened interface. *Nat. Mater.* **14**, 261–262 (2015).
32. Gin, S. *et al.* Origin and consequences of silicate glass passivation by surface layers. *Nat. Commun.* **6**, 6360–6368 (2015).
33. Plimpton, S. Fast parallel algorithms for short-range molecular dynamics. *J. Comput. Phys.* **117**, 1–19 (1995).
34. Delaye, J.-M. & Ghaleb, D. Combining two types of molecular dynamics for rapid computation of high-energy displacement cascades. II. application of the method to a 70-kev cascade in a simplified nuclear glass. *Phys. Rev. B* **71**, 224204 (2005).
35. Abbas, A., Delaye, J.-M., Ghaleb, D. & Calas, G. Molecular dynamics study of the structure and dynamic behavior at the surface of a silicate glass. *J. Non-Cryst. Solids* **315**, 187–196 (2003).
36. Shinoda, W., Shiga, M. & Mikami, M. Rapid estimation of elastic constants by molecular dynamics simulation under constant stress. *Phys. Rev. B* **69**, 134103 (2004).
37. Parrinello, M. & Rahman, A. Polymorphic transitions in single crystals: A new molecular dynamics method. *J. Appl. Phys.* **52**, 7182–7190 (1981).
38. Loewenstein, W. The distribution of aluminum in the tetrahedra of silicates and aluminates. *Am. Mineral* **39**, 92–96 (1954).
39. Ohkubo, T., Iwadate, Y., Deguchi, K., Ohki, S. & Shimizu, T. Changes in surface structure of sodium aluminoborosilicate glasses during aqueous corrosion analyzed by using nmr. *J. Phys. Chem. Solids* **77**, 164–171 (2015).
40. Cygan, R. T., Liang, J.-J. & Kalinichev, A. G. Molecular models of hydroxide, oxyhydroxide, and clay phases and the development of a general force field. *J. Phys. Chem. B* **108**, 1255–1266 (2004).
41. Kerisit, S., Liu, C. & Ilton, E. S. Molecular dynamics simulations of the orthoclase (001)- and (010)-water interfaces. *Geochim. Cosmochim. Acta* **72**, 1481–1497 (2008).
42. Berendsen, H. J. C., Grigera, J. R. & Straatsma, T. P. The missing term in effective pair potentials. *J. Phys. Chem.* **91**, 6269–6271 (1987).
43. Kusaka, I., Wang, Z.-G. & Seinfeld, J. Binary nucleation of sulfuric acid–water: Monte carlo simulation. *J. Chem. Phys.* **108**, 6829–6848 (1998).
44. Ryckaert, J.-P., Ciccotti, G. & Berendsen, H. J. Numerical integration of the cartesian equations of motion of a system with constraints: Molecular dynamics of n-alkanes. *J. Comput. Phys.* **23**, 327–341 (1977).
45. Tuckerman, M. E., Alejandre, J., López-Rendón, R., Jochim, A. L. & Martyna, G. J. A liouville-operator derived measure-preserving integrator for molecular dynamics simulations in the isothermal–isobaric ensemble. *J. Phys. A-Math. Gen.* **39**, 5629–5651 (2006).
46. Hoover, W. G. Canonical dynamics: Equilibrium phase-space distributions. *Phys. Rev. A* **31**, 1695–1697 (1985).
47. Hockney, R. W. & Eastwood, J. W. *Computer simulation using particles* (CRC Press, 1988).
48. Willems, T. F., Rycroft, C. H., Kazi, M., Meza, J. C. & Haranczyk, M. Algorithms and tools for high-throughput geometry-based analysis of crystalline porous materials. *Microporous Mesoporous Mater.* **149**, 134–141 (2012).
49. Pyykkö, P. & Atsumi, M. Molecular single-bond covalent radii for elements 1–118. *Chem. Euro. J.* **15**, 186–197 (2009).
50. Franks, F. *Water: A matrix of life*, vol. 21 (Royal Society of Chemistry, 2000).
51. Ohkubo, T., Ibaraki, M., Tachi, Y. & Iwadate, Y. Pore distribution of water-saturated compacted clay using nmr relaxometry and freezing temperature depression; effects of density and salt concentration. *Appl. Clay Sci.* **123**, 148–155 (2016).
52. Higgins, J. & Schlenker, J. A new family of mesoporous molecular sieves prepared with liquid crystal templates. *Nature* **331**, 698–699 (1988).
53. Everett, D. Iupac manual of symbols and terminology: Appendix 2, part 1: Colloid and surface chemistry. *Pure Appl. Chem.* **31**, 577–638 (1972).

54. Urata, S. *et al.* Molecular dynamics simulation of swollen membrane of perfluorinated ionomer. *J. Phys. Chem. B* **109**, 4269–4278 (2005).
55. Cui, S. *et al.* A molecular dynamics study of a nafion polyelectrolyte membrane and the aqueous phase structure for proton transport. *J. Phys. Chem. B* **111**, 2208–2218 (2007).
56. Venkatnathan, A., Devanathan, R. & Dupuis, M. Atomistic simulations of hydrated nafion and temperature effects on hydronium ion mobility. *J. Phys. Chem. B* **111**, 7234–7244 (2007).
57. Enderby, J. E. Ion solvation via neutron scattering. *Chem. Soc. Rev.* **24**, 159–168 (1995).
58. Skipper, N. & Neilson, G. X-ray and neutron diffraction studies on concentrated aqueous solutions of sodium nitrate and silver nitrate. *J. Phys. Cond. Matter* **1**, 4141 (1989).
59. Howe, M. The hydration of ions in aqueous solution: Reverse monte carlo analysis of neutron diffraction data. *J. Phys. Cond. Matter* **2**, 741–748 (1990).
60. Impey, R., Madden, P. & McDonald, I. Hydration and mobility of ions in solution. *J. Phys. Chem.* **87**, 5071–5083 (1983).
61. Roder, A., Kob, W. & Binder, K. Structure and dynamics of amorphous silica surfaces. *J. Chem. Phys.* **114**, 7602–7614 (2001).

Acknowledgements

The authors would also like to acknowledge the insightful contributions of Dr. J.-M. Delaye (Atomic Energy and Alternative Energies Commission).

Author Contributions

T.O. carried out the MD simulation and analysis, T.O., S.G., M.C. and Y.I. designed research and wrote the paper. All authors reviewed the manuscript.

Additional Information

Supplementary information accompanies this paper at <https://doi.org/10.1038/s41598-018-22015-3>.

Competing Interests: The authors declare no competing interests.

Publisher's note: Springer Nature remains neutral with regard to jurisdictional claims in published maps and institutional affiliations.



Open Access This article is licensed under a Creative Commons Attribution 4.0 International License, which permits use, sharing, adaptation, distribution and reproduction in any medium or format, as long as you give appropriate credit to the original author(s) and the source, provide a link to the Creative Commons license, and indicate if changes were made. The images or other third party material in this article are included in the article's Creative Commons license, unless indicated otherwise in a credit line to the material. If material is not included in the article's Creative Commons license and your intended use is not permitted by statutory regulation or exceeds the permitted use, you will need to obtain permission directly from the copyright holder. To view a copy of this license, visit <http://creativecommons.org/licenses/by/4.0/>.

© The Author(s) 2018